

Fault Damage Zone Effects on Ground Motions during the 2019 M_w 7.1 Ridgecrest, California, Earthquake

Te-Yang Yeh¹ and Kim B. Olsen^{*1}

ABSTRACT

We have simulated 0–3 Hz deterministic wave propagation in the Southern California Earthquake Center Community Velocity Model (CVM) version CVM-S4.26-M01 for the 2019 M_w 7.1 Ridgecrest earthquake. A data-constrained high-resolution fault zone model (Zhou *et al.*, 2022) is incorporated into the CVM to investigate the effects of the near-fault low-velocity zone (LVZ) on the resulting ground motions, constrained by strong-motion data recorded at 161 stations. The finite-fault source used for the simulation of the Ridgecrest event was obtained from the Liu *et al.* (2019) kinematic inversion, enriched by noise following a von Karman correlation function above ~ 1 Hz with a f^{-2} high-frequency decay. Our results show that the heterogeneous near-fault LVZ inherent to the fault zone structure significantly perturbs the predicted wave field in the near-source region, in particular by more accurately generating Love waves at its boundaries. The fault zone decreases the 0.1–0.5 Hz mean absolute Fourier amplitude spectrum bias to seismic recordings for all sites in the model and in the Los Angeles basin area (~ 200 km from the source) by 16% and 26%, respectively. The fault zone structure generally improves modeling of the long-period features in the data and lengthens the coda-wave trains, in better agreement with observations. The favorable fit to data was obtained with a model including high-resolution surface topography, a 700-m-thick geotechnical layer and frequency-dependent anelastic attenuation in the model domain, with $Q_S = 0.1V_S$ and $Q_S(f) = 0.1V_S f^{0.5}$ (V_S in m/s) for frequencies lower and higher than 1 Hz, respectively. We recommend that a data-constrained fault zone velocity structure, where available, be included in ground-motion modeling to obtain the least-biased fit to observed seismic data.

KEY POINTS

- We merge a high-resolution Ridgecrest area fault zone model with a widely used Community Velocity Model.
- Including the fault zone structure generally improves the fit of synthetic time histories to observations.
- Ground-motion modeling should include fault zone structure, where available, for least-biased results.

Supplemental Material

INTRODUCTION

A fault damage zone structure is usually characterized as a low-velocity zone (LVZ) surrounding a fault plane, embedded in host rock with higher seismic wavespeeds. Numerical modeling studies have shown that the velocity contrast at the boundaries of the damage zone can generate trapped waves, an important signature of fault zones (Li and Leary, 1990; Ben-Zion *et al.*, 2003; Lewis *et al.*, 2005). Fault zone trapped waves have been found to increase the near-fault ground motions

(Ben-Zion and Aki, 1990; Spudich and Olsen, 2001; Peng and Ben-Zion, 2006), and numerical simulations have been used to reconstruct the near-fault wave field in the presence of a damage structure (Li and Leary, 1990; Li *et al.*, 1990; Igel *et al.*, 2002; Fohrmann *et al.*, 2004). These studies suggest that the fault damage zone structures are capable of significantly modulating the wave field from earthquakes.

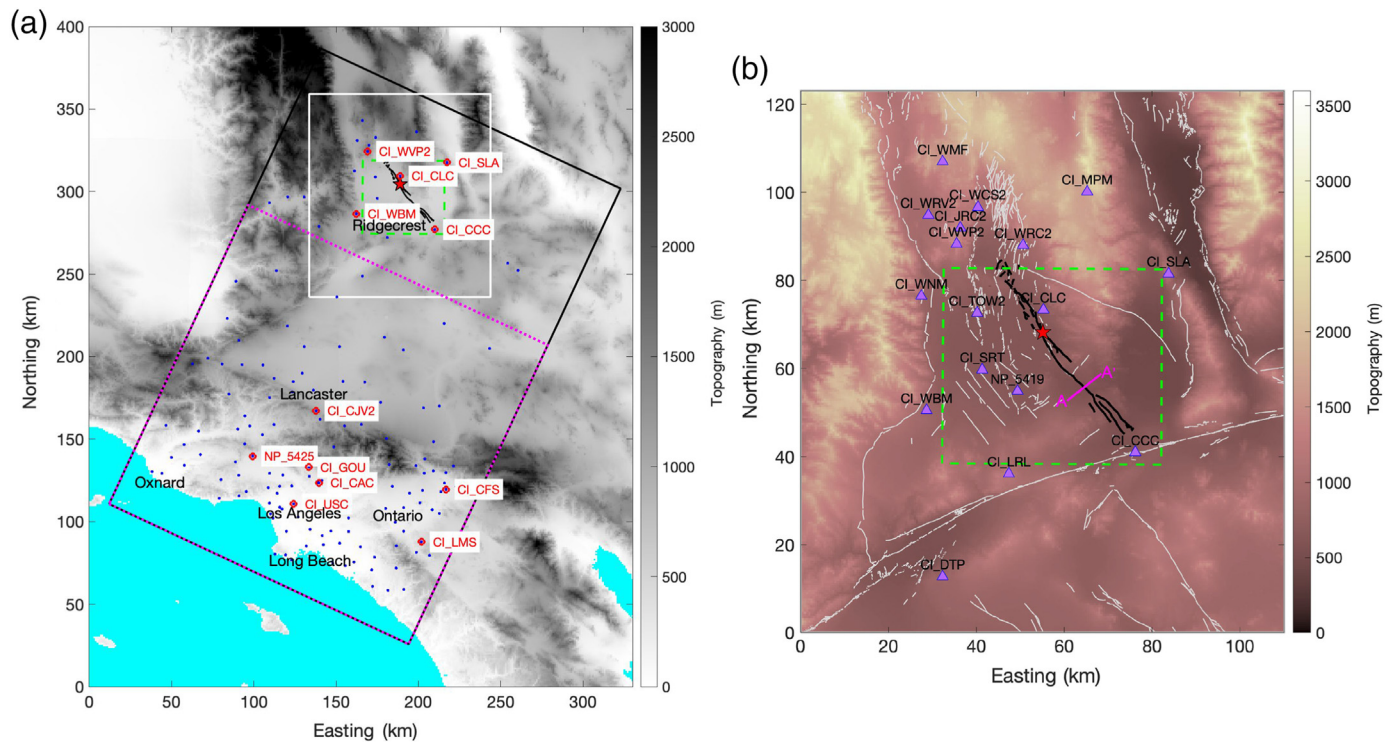
Because of the limited constraints on the 3D geometry and velocities of fault zone structures, previous numerical studies of fault zone effects included considerable simplification. For example, Roten *et al.* (2018, 2014) and Graves and Pitarka (2016) described the damage zone generically by reducing the

1. Department of Geological Sciences, San Diego State University, San Diego, California, U.S.A., <https://orcid.org/0000-0002-9146-6804> (T.-Y.); <https://orcid.org/0000-0002-3078-485X> (KBO)

*Corresponding author: kbolsen@sdsu.edu

Cite this article as Yeh, T.-Y., and K. B. Olsen (2023). Fault Damage Zone Effects on Ground Motions during the 2019 M_w 7.1 Ridgecrest, California, Earthquake, *Bull. Seismol. Soc. Am.* **113**, 1724–1738, doi: [10.1785/0120220249](https://doi.org/10.1785/0120220249)

© Seismological Society of America



shear-wave velocities by 30%–50% within a predefined width (100–400 m), usually located symmetrically around the fault (Vidale and Li, 2003; Li et al., 2004; Cochran et al., 2009), and the fault geometry was typically approximated as a simple vertical plane. Moreover, existing Community Velocity Models (CVMs), such as those developed by the Southern California Earthquake Center (SCEC), do not accurately resolve fault damage zones. For these reasons, the effects of including detailed fault zone structures on broadband ground motions from simulation studies are not yet fully understood.

To better understand the effects on ground motions from realistic damage zones with complex spatial variation, efforts have been made to image the velocity structure of fault zones (Li and Leary, 1990; Scott et al., 1994; Allam et al., 2014; Zhou et al., 2022). Specifically, Zhou et al. (2022) obtained a 3D high-resolution shear-wave velocity model for the region surrounding the faults that ruptured during the 2019 M_w 7.1 Ridgecrest, California, earthquake, using ambient noise tomography. Previous studies have simulated 3D wave propagation in the original SCEC CVMs and discussed the effects of source rupture process on near-source ground motions (Hirakawa and Barbour, 2020; Pitarka et al., 2021). Here, we simulate 0–3 Hz 3D wave propagation for the M_w 7.1 Ridgecrest earthquake to examine the effects of the fault damage zone imaged by Zhou et al. (2022), incorporated into the larger-scale SCEC CVM-S.4.26.M01 (Small et al., 2017), which is hereafter referred to as CVM-S. Specifically, we perform a set of wave propagation simulations to isolate the effects of the fault zone structure on the resulting ground motions and compare this with strong-motion records from the event. To estimate the most accurate seismic response of the fault zone, we first calibrate the parameters of the near-

Figure 1. (a) Model domain (large rectangle) for the simulations. Dots show locations of stations where seismic recordings of the 2019 Ridgecrest M_w 7.1 earthquake have been used in this study. Highlighted stations with names are used for waveform comparisons. The dashed box depicts the domain for which the fault zone structure was imaged by Zhou et al. (2022). The dotted square marks the area used to show peak ground motions in Figure 10. Thick traces are faults that ruptured in the 2019 M_w 7.1 Ridgecrest earthquake. (b) Near-source region inside the white square in panel (a), where triangles show the locations of stations used for analysis of near-source ground motions. The color version of this figure is available only in the electronic edition.

surface geotechnical layer (GTL) and frequency-dependent anelastic attenuation parameters using wave propagation distances >250 km.

This article is arranged as follows. We first introduce our numerical method and describe how we embed the high-resolution fault zone structure into the SCEC CVM-S. Then we present our approach to enrich a finite-fault source model obtained from a kinematic inversion, which we used for our wave propagation simulations, in spectral energy at frequencies above 1 Hz. We summarize our calibration of the GTL and the anelastic attenuation model for the simulations of the M_w 7.1 Ridgecrest earthquake. Finally, we compare the wavefields simulated with and without the fault zone structure and demonstrate its contribution to the resulting ground motions in time and frequency domains.

VELOCITY MODEL

Regional model and fault zone structure

Our simulations used a 200 km × 300 km model domain (the largest rectangle in Fig. 1a) with a depth extent of ~150 km. This domain accommodates both the source area for the 2019

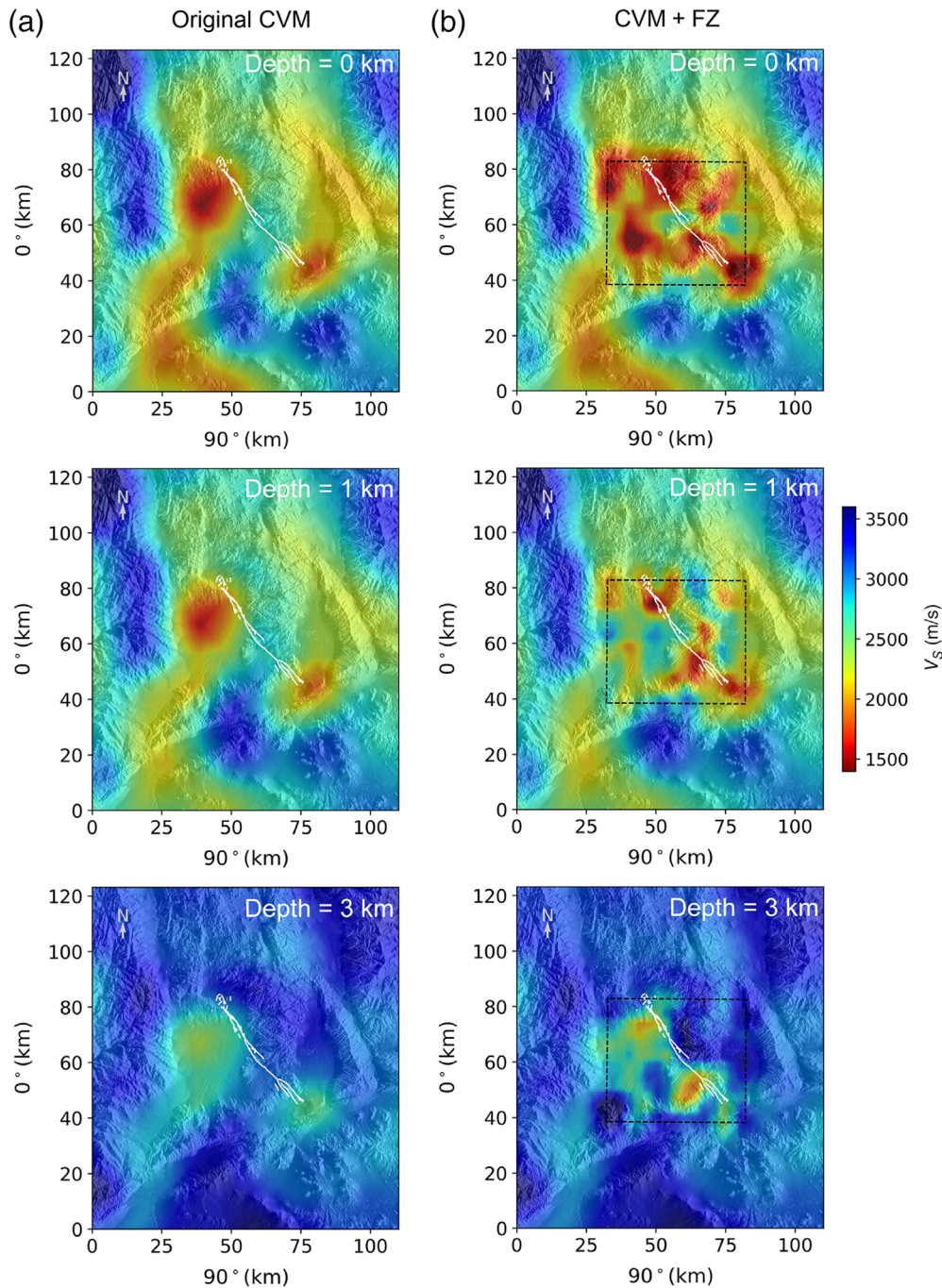


Figure 2. Comparison of horizontal slices of V_S inside the region shown in Figure 1b at different depths (a) without and (b) with incorporating the fault zone structure. The rectangle depicts the imaging domain of the fault zone model. Note that the slices do not include the geotechnical layer (GTL). CVM, community velocity model; FZ, fault zone. The color version of this figure is available only in the electronic edition.

Ridgecrest earthquake sequence and part of the greater Los Angeles region to the south. The seismic velocity and density information was extracted from the SCEC CVM-S. The choice of CVM-S is based on the results by [Taborda et al. \(2016\)](#), who found that this model generated ground motions with the best fit to data for a series of small earthquakes compared with another widely used CVM.

The 3D fault zone structure was imaged by [Zhou et al. \(2022\)](#) in a $50 \text{ km} \times 45 \text{ km}$ (dashed box in Fig. 1a,b) by 5 km volume. The model was inverted from seismic data recorded by a data set consisting of a coarse regional array and 2D dense arrays across the faults that ruptured during the 2019 M_w 6.4 and the M_w 7.1 Ridgecrest events ([Catchings et al., 2020](#)). [Zhou et al. \(2022\)](#) used the locally sparse tomography (LST) technique ([Bianco and Gerstoft, 2018](#); [Bianco et al., 2019](#)) and performed ambient noise cross correlation to measure Rayleigh-wave group velocities and estimated their dispersion curves. The 3D shear-wave velocity model was then inverted from the Rayleigh-wave group velocity dispersion curves. The LST method is capable of resolving both smooth and sharp contrasts in an earth model ([Bianco et al., 2019](#); [Zhou et al., 2022](#)), which are features inherent to fault zone structures. Specifically, the fault zone associated with the Ridgecrest ruptures is characterized by strong spatial heterogeneities (Fig. S1, available in the supplemental material to this article), as well as a low-velocity flower structure (Fig. S2).

Because the fault zone model obtained from ambient noise tomography only provides 3D shear-wave velocity (V_S) structure, we used the empirical relations from [Brocher \(2005\)](#) to compute P -wave velocities (V_P) and densities. To ensure smooth transitions between CVM-S and the fault zone model, we adopted the merging method proposed by [Ajala and Persaud \(2021\)](#) with a 15 km horizontal tapering width along the sides and a 600 m vertical transition zone at the bottom of the fault zone domain. Horizontal slices of V_S in Figure 2 reveal, as expected, higher spatial complexity in the fault zone model surrounding the faults

compared with CVM-S (see also vertical profiles of V_p , V_s , and density in Fig. S3). The lowest surface V_s within the imaged fault zone model is around 1100 m/s compared with a minimum surface V_s of 1400 m/s in the same area of CVM-S. It is important to avoid artificial velocity contrasts between the fault zone model and the CVM to minimize numerically induced reflected waves. Both depth slices (Fig. 2) and vertical profiles (Fig. S3) suggest that our combined model is sufficiently smooth where the two models intersect.

Broadband source model

Several rupture models for the 2019 M_w 7.1 Ridgecrest earthquake have been proposed using kinematic inversion (Liu *et al.*, 2019; Chen *et al.*, 2020; Goldberg *et al.*, 2020; Wang *et al.*, 2020). From trial-and-error modeling, we proceeded with a model from the kinematic inversion of seismic and geodetic data by Liu *et al.* (2019), which generated the least-biased ground-motion predictions (not shown here). The slip distribution and rupture times for the rupture model consisting of four planar segments are shown in Figure S4. However, because of limited temporal resolution often characterizing kinematic inversion results, the spectral energy of the source is deficient at frequencies above ~ 1 Hz. Various approaches have been proposed to calculate high-frequency signal with realistic energy levels, such as hybrid methods combining deterministic low- and stochastic high-frequency synthetics (e.g., Olsen and Takedatsu, 2014; Graves and Pitarka, 2016; Pitarka *et al.*, 2021). Here, to preserve the data-constrained low-frequency source model and to avoid potential artifacts at frequencies where the deterministic and stochastic signals are merged, we propose a different method to enhance the seismic energy above the highest frequency resolved by the kinematic inversion. The enhancement is done by simply perturbing the moment rate functions of all the subfaults with noise following a von Karman correlation function, in which the Fourier amplitude spectrum (FAS) is

$$P_{vk}(f) = \frac{2\sqrt{\pi}T_c\varepsilon^2\Gamma(\nu+1/2)^{\nu+1/2}}{\Gamma(\nu)(1+(T_c f)^2)}, \quad (1)$$

in which T_c is a characteristic time controlling the corner frequency of the spectrum; ε is the root mean square fluctuation; Γ denotes the Gamma function; and ν is the Hurst number, which was arbitrarily set to be 0.05. Figure 3a illustrates this spectral enhancement procedure for a single subfault. The generated noise is normalized by its standard deviation in the time domain such that it follows the standard normal distribution ($P_{vk}(t)$ in Fig. 3a), which makes it straightforward to rescale for different standard deviations. The enhanced moment rate function is derived by multiplying the moment rate function from the inverted model ($s(t)$ in Fig. 3a) with a perturbation function, that is

$$s_{HF}(t) = s(t) \times (1 - \sigma \times P_{vk}(t)), \quad (2)$$

in which s_{HF} is the enhanced moment rate function and σ is the standard deviation. This approach ensures that the rupture time of a subfault remains the same, and we used normalization to ensure the scalar moment of the subfault is unchanged after adding the random noise. The same procedure is then repeated for noise with different random seed numbers applied to all the subfaults. We used grid search to find the characteristic time and standard deviation for the von Karman noise that generated a moment rate spectrum accumulated for all the subfaults with the best fit to the targeted source spectrum of the form

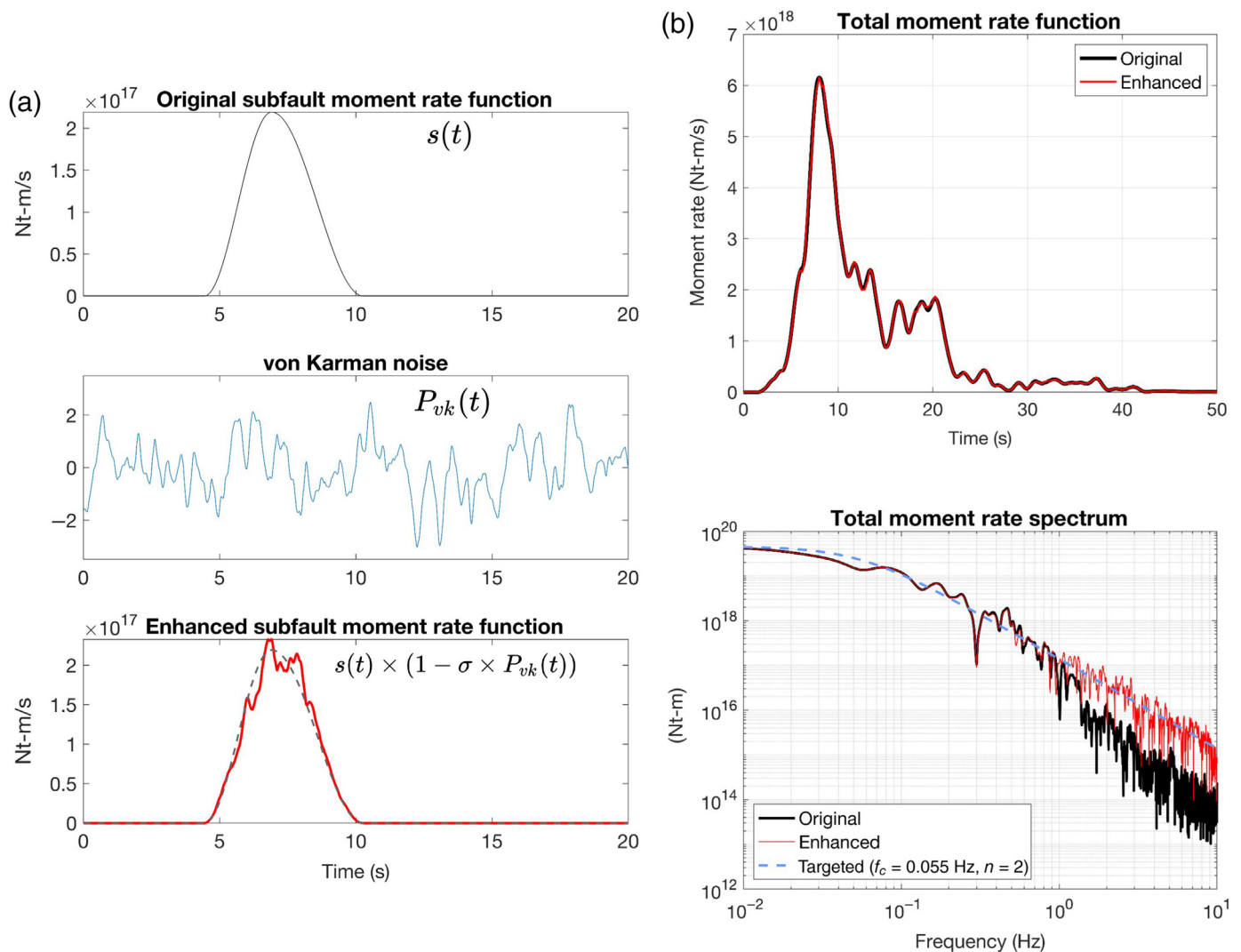
$$M(f) = \frac{M_0}{1 + (f/f_c)^n}, \quad (3)$$

in which M_0 is the seismic moment, n is the fall-off rate of the higher frequencies, and f_c is the corner frequency (Brune, 1970). The corner frequency here is 0.055 Hz, computed from the total moment rate function of the source model. Figure 3b compares the total moment rate functions with and without the enhancement in time and frequency domains. The moment rate function is essentially unchanged, whereas the total moment rate spectrum decays following the targeted spectral shape with a f^{-2} rolloff rate after the enhancement, assuming $n = 2$ in equation (3). For the Liu *et al.* (2019) source model, we found that von Karman noise generated with a characteristic time $T_c = 0.11$ s and standard deviation $\sigma = 0.1$ provided the best fit to the targeted source spectrum.

Wave propagation method

We performed 3D numerical wave propagation simulations using the highly scalable code AWP-ODC (Anelastic Wave Propagation–Olsen, Day, and Cui, named after the three main authors), which solves the velocity–stress wave equation with an explicit staggered-grid finite-difference scheme (Olsen, 1994; Cui *et al.*, 2010, 2013). This graphic processing unit-enabled code is fourth-order accurate in space and second-order accurate in time. The code takes advantage of a discontinuous mesh technique with a change in grid spacing by a factor of 3 between domains vertically, which significantly reduces the memory use (Nie *et al.*, 2017). The curvilinear mesh was used in the shallowest mesh block of the domain to include the effects of surface topography (O’Reilly *et al.*, 2021). To minimize computational requirements, we clamped the lowest shear-wave velocities at 300 m/s. To achieve a maximum frequency of 3 Hz with a minimum shear-wave speed of 300 m/s using at least 6.7 grid points per minimum wavelength, the smallest grid spacing in our simulations was set to 15 m (O’Reilly *et al.*, 2021). See Table 1 for technical details of the numerical simulations.

Hu *et al.* (2022b) described a method to incorporate an approximate contribution of the near-surface low-velocity materials ($V_s < 300$ m/s in this case), often omitted in 3D deterministic simulations to save computational resources. In this method, the vertically incident *SH*-wave transfer



functions for the V_S profile with and without the near-surface low-velocity materials were computed to form a spectral correction function. Here, we corrected the Fourier amplitude spectra for the two horizontal components to incorporate an approximation of the effects of the material with $V_S < 300$ m/s. In general, this effect on the ground motions was negligible within the analyzed frequency band in our case (see Fig. S5).

Data processing

The ground motions of the M_w 7.1 Ridgecrest event have been well recorded by networks of densely distributed seismic stations throughout the simulation domain. We use acceleration data from HN channels at stations operated under networks CI and NP (see [Data and Resources](#) for more details). The poles and zeros for each channel were used to remove the instrument response, and the acceleration waveforms were integrated once to get velocity waveforms. Baselines of the near-fault records (stations shown in Fig. 1b) were corrected using the method proposed by [Wang et al. \(2011\)](#). Prior to the validations, all

Figure 3. Enhancement of spectral energy for the source model from the kinematic source inversion. (a) Moment rate function for (top) one subfault, (middle) von Karman correlated noise with T_c of 0.11 s, and (bottom) comparison of original and the perturbed moment rate function with $\sigma = 0.1$. (b) Comparison of the total moment rate functions in the (top) time and the (bottom) frequency domain, respectively, for which the targeted total moment rate spectrum is shown by the dashed curve in the bottom panel. The color version of this figure is available only in the electronic edition.

observed and simulated data were band-pass filtered between 0.02 and 3 Hz using two forward passes of a (causal) second-order Butterworth filter. In total, 161 stations were included in our analysis.

GTL and $Q(f)$ model

V_S of the top ~ 30 m of Earth's crust is often relatively well constrained from borehole and geotechnical data ([Yong et al., 2013](#)), or it can be estimated as a proxy from topographic surface elevation ([Wald and Allen, 2007](#)). Similarly, velocities

TABLE 1
Simulation Details

Domain	
Length	200.87 km
Width	304.55 km
Depth	149.61 km
Southwest corner	-119.50000°, 34.00000°
Northwest corner	-118.14120°, 36.50876°
Southeast corner	-117.52448°, 33.25866°
Northeast corner	-116.11682°, 35.74564°
Spatial Resolution	
Grid spacing	15 m: free surface to 11.97 km below sea level
	45 m: 11.87–24.78 km below sea level
	135 m: 24.47–149.61 km below sea level
Maximum frequency	3 Hz
Minimum V_S	300 m/s
Points per minimum wavelength	6.66
Temporal Resolution	
Timestep	0.0008 s
Simulation time	180 s
Miscellaneous	
Geotechnical tapering depth	700 m

of the layers below ~1000 m depth can be constrained by tomographic results. On the other hand, in particular for rock sites, the velocities between these two regions are often poorly resolved, as is the case for CVM-S. To alleviate this issue, Boore and Joyner (1997) used generic models to bridge the gap between data constraints in the two regions, and Ely *et al.* (2010) proposed a scheme that determines the shallow V_S by interpolation (“tapering”) between the V_{S30} value and the original tomography model at a certain depth (z_T). Here, we describe the near-surface seismic velocities using the approach by Hu *et al.* (2022b), who showed that simulations of the 2014 M_w 5.1 La Habra, California, earthquake, generated better fit to data using larger values of z_T compared with the 350 m recommended by Ely *et al.* (2010). Consistent with Hu *et al.* (2022b) but not Ely *et al.* (2010), we only modified the velocities and densities when the existing V_S is higher than that given by the taper, ensuring that the (generally better constrained) low velocities in the basins of the existing model will remain in the model (e.g., low-velocity basin materials in Los Angeles). We used trial-and-error simulations to estimate the tapering depth of the GTL that provided the least-biased fit to the ground-motion data (see discussion in the supplemental material and Figs. S6 and S7 for further details of the analysis).

A popular procedure for parameterizing the Q model, adopted in many earlier numerical wave propagation studies, consists of using linear or polynomial relationships between Q and the local V_S values (Olsen *et al.*, 2003; Taborda and Bielak, 2013, 2014; Lai *et al.*, 2020; Pitarka *et al.*, 2021). As frequency

increases beyond ~1 Hz, strong-motion data in some regions indicate that the seismic attenuation becomes frequency dependent (Aki, 1980; Raouf *et al.*, 1999; Phillips *et al.*, 2014; Wang and Shearer, 2017), which can be captured by numerical schemes (Withers *et al.*, 2015). The AWP-ODC supports frequency-dependent attenuation that follows a power-law description:

$$Q_s(f) = Q_{s,0}, \quad f < f_0,$$

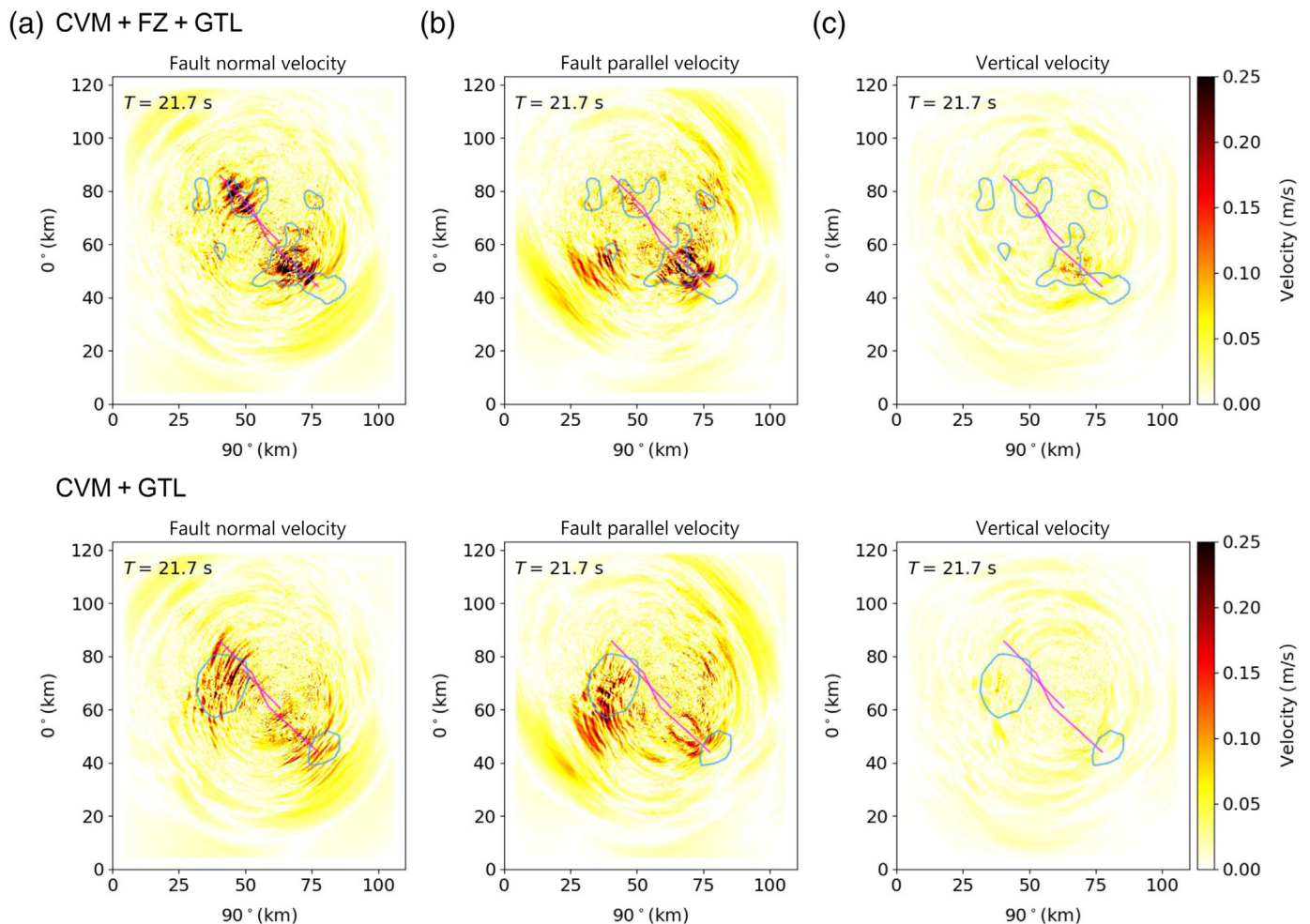
$$Q_s(f) = Q_{s,0} \left(\frac{f}{f_0} \right)^\gamma, \quad f \geq f_0, \quad (4)$$

in which we assumed that the transition frequency f_0 is 1 Hz, $Q_{s,0}$ is a constant Q_S value, and the power-law exponent γ controls the rate of increase for Q_S above 1 Hz (Withers *et al.*, 2015). Following the format of Olsen *et al.* (2003), we assumed a constant Q_S to local V_S ratio ($\frac{Q_{s,0}}{V_S} = k$), and therefore the parameters to be estimated are k and γ in equation (4). We furthermore assumed $Q_P = 2Q_S$, following Olsen *et al.* (2003).

The 0–5 Hz deterministic simulations of the 2014 M_w 5.1 La Habra, California, earthquake by Hu *et al.* (2022a) found optimal ranges of $k = 0.075$ – 0.1 and $\gamma < 0.6$ for the greater Los Angeles area. Because our model area is larger than the region used by Hu *et al.* (2022a), including an additional section of the Sierra Nevada Mountains, we re-evaluated the optimal attenuation relation (see discussion in supplemental material and Figs. S8–S11). Using trial-and-error simulations with a series of tapering depths of the GTL, we find optimal results for a 700-m-thick GTL and $Q(f)$ with $Q_S = 0.1V_S$ and $Q_S(f) = 0.1V_S f^{0.5}$ (V_S in m/s) for frequencies lower and higher than 1 Hz, respectively. Lacking fault-specific constraints for the Ridgecrest area, this $Q(f)$ model is applied inside the fault zone model as well as the broader CVM. These parameters are used in the following simulations examining the effects of the Ridgecrest fault zone on the resulting ground motions. See discussion in supplemental material and Figures S8–S11 for further detail of the optimization of the anelastic attenuation parameters.

Effects on ground motions from the fault zone structure

After calibration of the GTL and attenuation model, we carried out simulations to investigate the effects of the fault zone on the resulting ground motions. Figure 4 demonstrates significant differences in the surface velocity wavefield between simulations with (CVM + FZ + GTL) and without (CVM + GTL) the fault zone structure, inside the domain outlined by the white box in Figure 1a. When including the fault zone, the wave fronts exhibit a more complex pattern surrounding the ruptured faults with higher amplitudes compared with the model without the fault zone. The differences can be attributed to waves generated by the velocity contrast between the LVZs



around the faults in the imaged fault zone structure and the surrounding host rock (Fig. S1). The spatial complexities in the fault zone structure lead to less coherent wave fronts and longer-lasting wave energy near the causative faults, explaining the prolonged coda wave trains in the corresponding synthetic waveforms. The increased particle velocities correlate well with locations above the near-fault LVZ at 1 km depth (see Fig. 4a). The snapshots also show that the fault zone amplification effects persist beyond the fault LVZ, specifically through Love waves propagating to the south (see fault-parallel velocity in Fig. 4).

Figure 5 illustrates the contributions of the fault zone on the resulting peak ground velocities (PGVs) and peak ground accelerations (PGAs) from the M_w 7.1 Ridgecrest earthquake. These maps emphasize how the fault zone significantly increases the PGVs and PGAs by up to a factor of 3 toward the southeastern end of the fault, specifically in bands aligned along and perpendicular to the fault traces. The increase in PGV as well as coda duration due to the fault zone is further illustrated by comparison of synthetic time histories with and without the LVZ across the fault zone (see Fig. 6). The maximum PGV and PGA values predicted in the near-fault area are about 60 cm/s and 0.6g, respectively.

Figure 4. Snapshots of absolute particle velocity along (a) fault normal, (b) fault parallel, and (c) vertical directions in the near-fault region (Fig. 1b) for simulations including the GTL and with (top) and without (bottom) the imaged fault zone model. The northwest–southeast-trending lines depict the fault trace used for simulating the M_w 7.1 Ridgecrest event. The contours depict V_S of 2100 m/s at 1 km below the free surface in the corresponding models. Animations of the wave propagation can be found in the supplemental material. The color version of this figure is available only in the electronic edition.

The effects of the fault zone on the resulting ground motions shown above include a calibrated GTL and $Q(f)$, perhaps the most realistic reference. However, because both the GTL and the fault zone structure add low-velocity material to the model, we also illustrate the effects of the fault zone relative to the CVM-S without the GTL in the simulated ground motions in the near-source area in Figure 7. The areas of significant PGVs and PGAs are greatly expanded to include the southeastern and northwestern parts of the fault system because of amplification effects in the LVZ.

Comparison of snapshots (see Fig. 8) and animations (see animations in the supplemental material) from simulations using models including the GTL with (CVM + FZ + GTL)

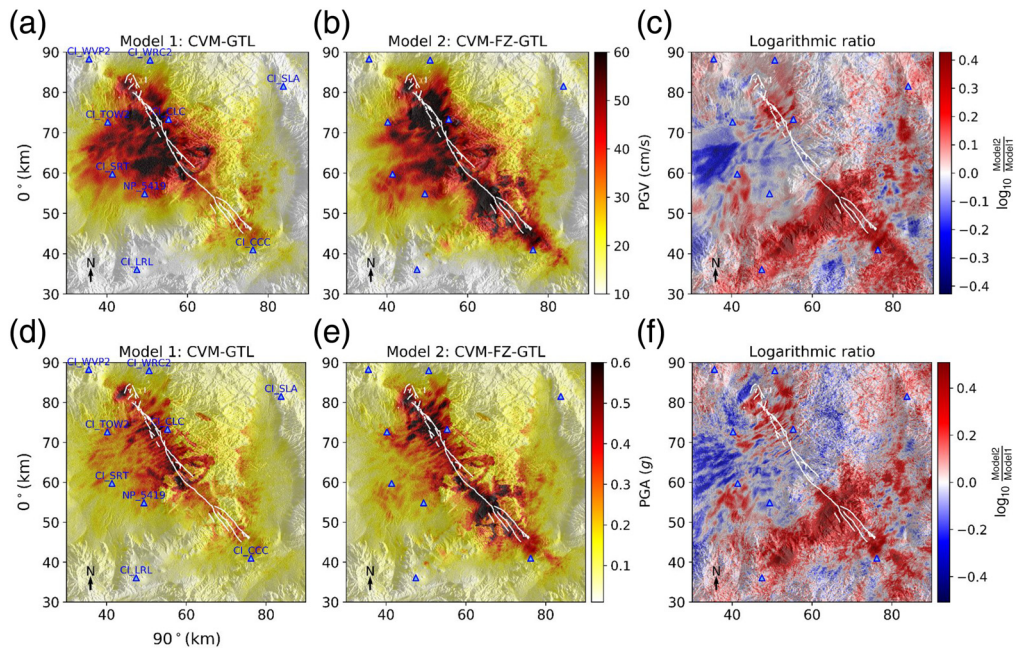


Figure 5. (a,b) Peak ground velocities (PGVs) and (d,e) peak ground accelerations (PGAs) in the near-fault region (see Fig. 1b for location) for models (left) Community Velocity Model (CVM-GTL) and (center) CVM-FZ-GTL along with the

logarithmic ratio (c,f). Lines depict fault traces that ruptured during the M_w 7.1 Ridgecrest event. Triangles depict stations used for waveform comparison. The color version of this figure is available only in the electronic edition.

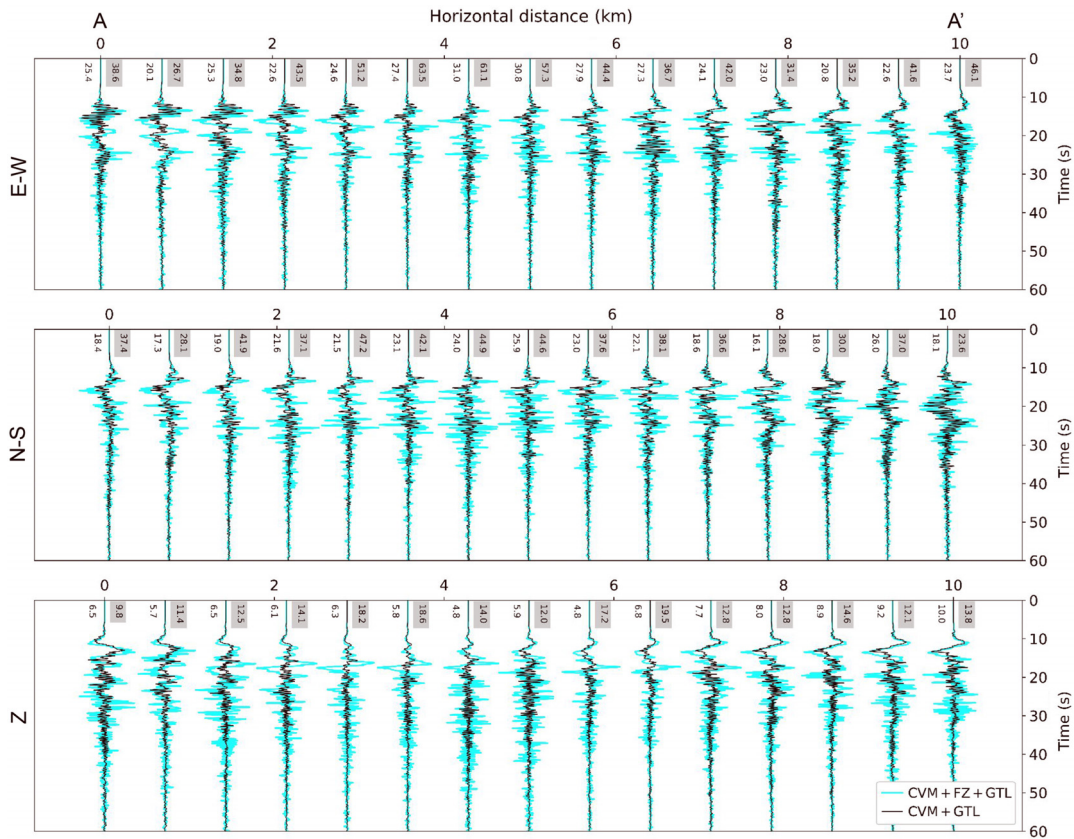
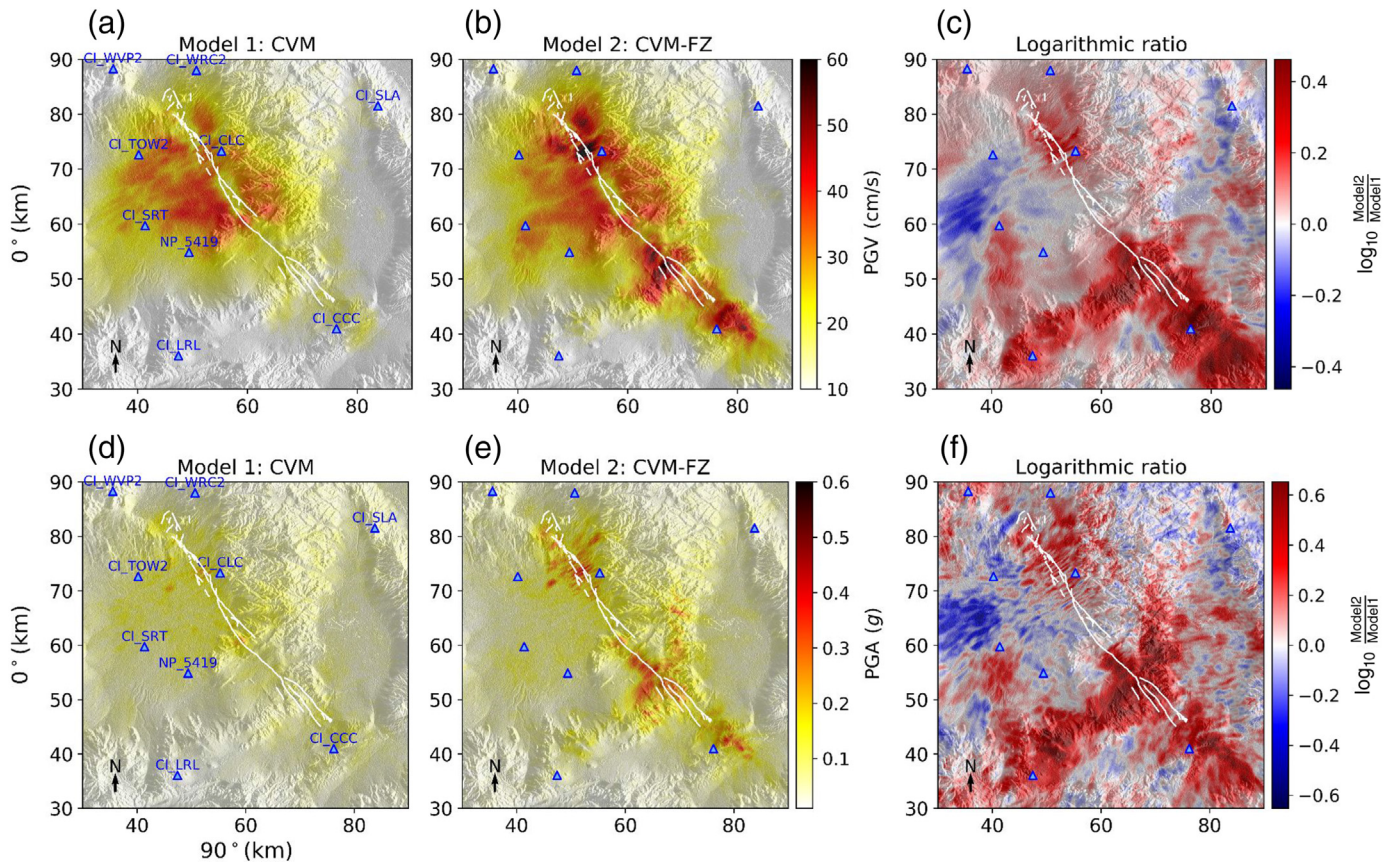


Figure 6. Three-component record section of velocity waveforms along a profile across the fault (see profile A–A' in Fig. 1b) for the model with (CVM + FZ + GTL, thick traces) and without (CVM + GTL, thin traces) the fault zone

structure. Peak velocities in centimeters per second for models with (shaded) and without the fault structure are shown at the beginning of each record. The color version of this figure is available only in the electronic edition.



and without (CVM + GTL) the fault zone farther from the source shows additional evidence that the fault zone generates a more complicated wavefield because the trapped waves generated within the LVZ continue to contribute wave energy after the termination of the source rupture. In particular, the snapshots show surface-wave trains with amplitude and duration amplified by the LVZ at distances along the paths to the Ventura and Los Angeles basins. The snapshots and movies clearly reveal that the fault zone increases the coda duration in the synthetics. In addition, the record section of synthetic velocity time series between the epicenter and station CI_GOU shown in Figure 9 illustrates the efficacy of the model with the fault zone to generate large-amplitude surface waves (indicated by the dashed line).

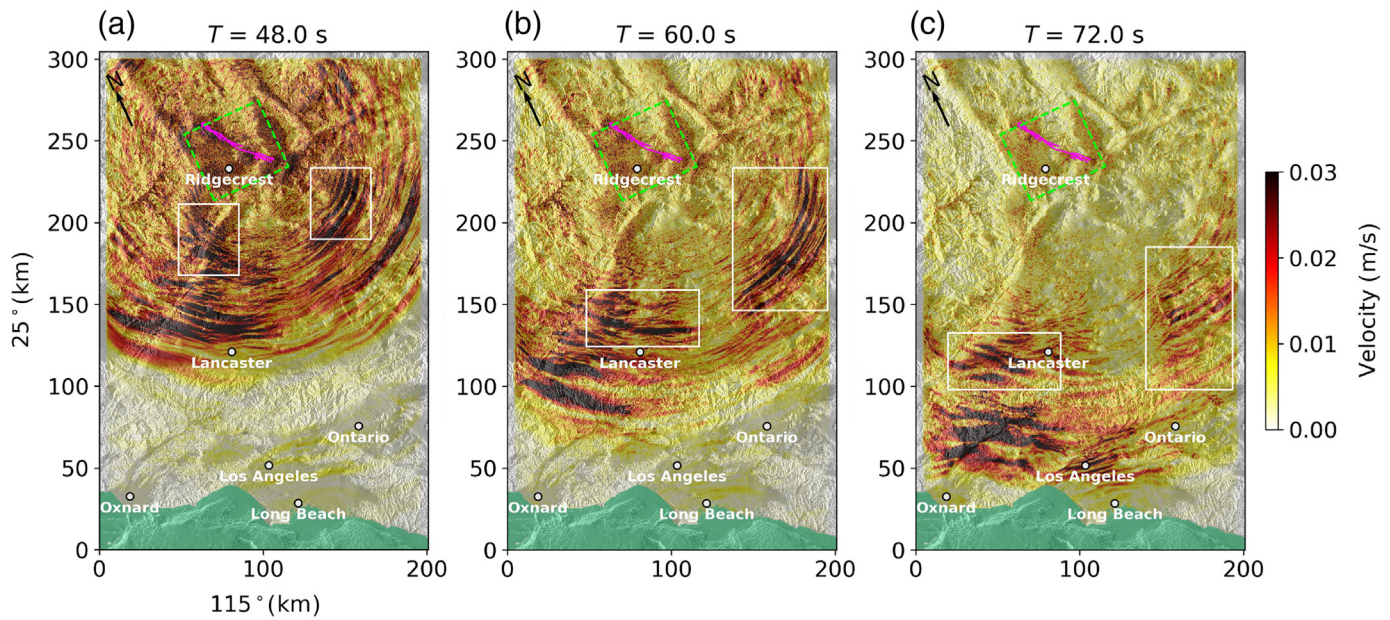
The PGVs are notably increased (by $\leq 25\%$) within the Los Angeles basin because of the addition of the fault zone structure (Fig. 10). The model without the fault zone primarily generates a band of amplified PGVs in the southeastern part of the basin. On the other hand, the fault zone tends to distribute part of this energy into increased PGVs in most other parts of the basin, in particular toward the northwest. This is likely caused by a less coherent wavefield broken up by the heterogeneous fault zone. The fault zone structure only slightly amplifies the PGAs (Fig. 10).

The seismic data recorded in our model area from the M 7.1 Ridgecrest earthquake generally support the model including the

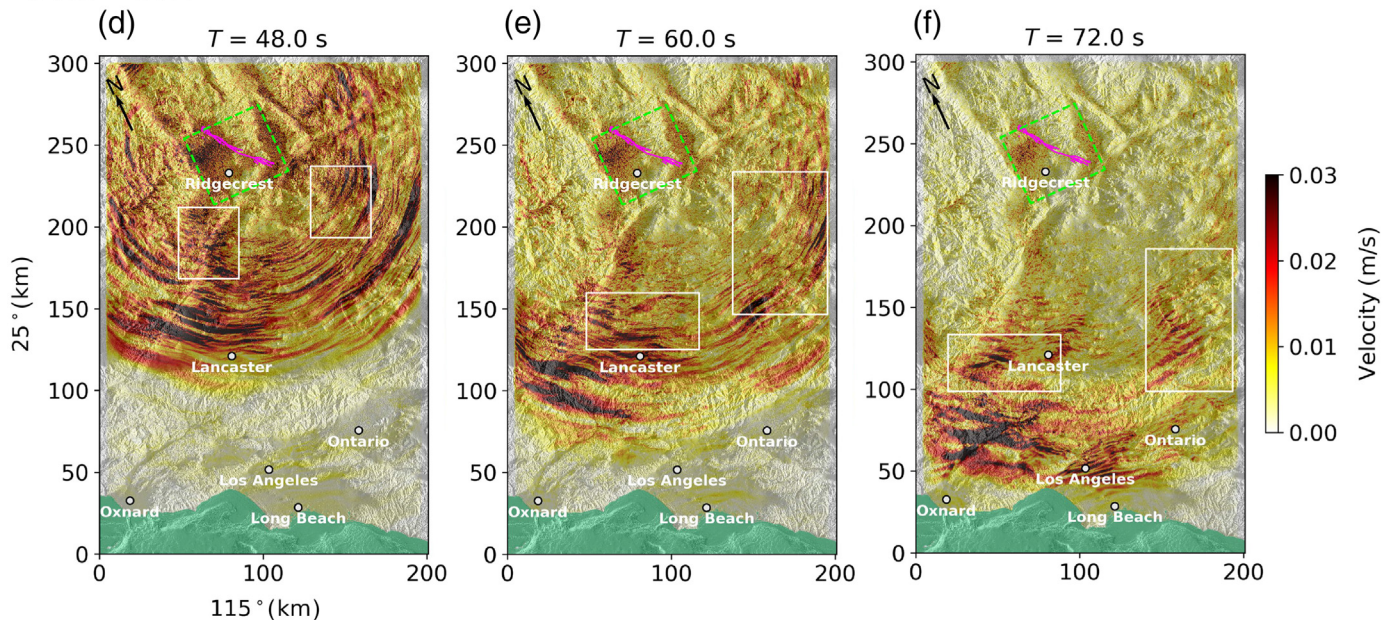
Figure 7. (a,b) PGVs and (d,e) PGAs in the near-fault region (see Fig. 1b for location) for models without (CVM) and with (CVM-FZ) the fault zone (but without the GTL). (c,f) Maps of the ratio between peak motions with and without the fault zone (note log scale). Lines depict fault traces that ruptured during the M_w 7.1 Ridgecrest event. The color version of this figure is available only in the electronic edition.

fault zone both near and far from the source. For example, the large-amplitude phases at CI_CCC in Figure 11 and at farther distances (CI_CJV2 and NP_5425 in Fig. 11) including the fault zone show an improved correlation with data compared with the synthetics without the fault zone. The goodness-of-fit (GOF) curves using FAS (see supplementary material, equations S1 and S2) demonstrate that the fault zone improves the spectral fit between 0.1 and 0.5 Hz, primarily on the east–west and the vertical components (see Fig. 12b). For all seismic recordings inside our model domain, we find that including the fault zone decreases the 0.1–0.5 Hz mean absolute FAS bias to seismic recordings for all sites by 16% and specifically for the greater Los Angeles basin (inside white box in Fig. 10) by 26%. In the absence of the GTL, the LVZ still improves the GOF of the FAS (Fig. 12a). The model with the GTL but without the fault zone results in substantial enhancement of spectral energy at frequencies >0.5 Hz, decreasing the bias of the seismic response at higher frequencies (see also Fig. S12). Additional comparisons including

CVM + FZ + GTL



CVM + GTL



waveforms, cumulative absolute velocity, and FAS can be found in the supplemental material (Figs. S13–S17 for near-source stations and Figs. S18–S23 for stations farther from the source).

In addition to the fault zone and GTL, surface topography and 3D basin structure affect the ground motions from our simulations of the M_w 7.1 Ridgecrest earthquake. Distributions of both PGV and PGA (Fig. 10) are amplified on the peaks and ridges in the southern Sierra Nevada (northern parts of the maps) along the western part of the Mojave Desert and into the Ventura basin. The high-velocity material of the San Bernardino Mountains experiences relatively small ground motions before the waves are amplified by the sediments of the Los Angeles basin further to the south.

Figure 8. Snapshots of the norm of the particle velocity (a–c) with and (d–f) without the fault zone model. The dashed box is the domain where the fault zone structure was imaged. The white boxes depict areas where the fault zone significantly affects the particle velocities. The color version of this figure is available only in the electronic edition.

DISCUSSION AND CONCLUSIONS

We have simulated 0–3 Hz 3D deterministic wave propagation for the 2019 M_w 7.1 Ridgecrest, California, earthquake in a 200 km × 300 km domain from the source region into the Los Angeles basin. Strong-motion data recorded by a dense deployment of seismic stations were then used to estimate

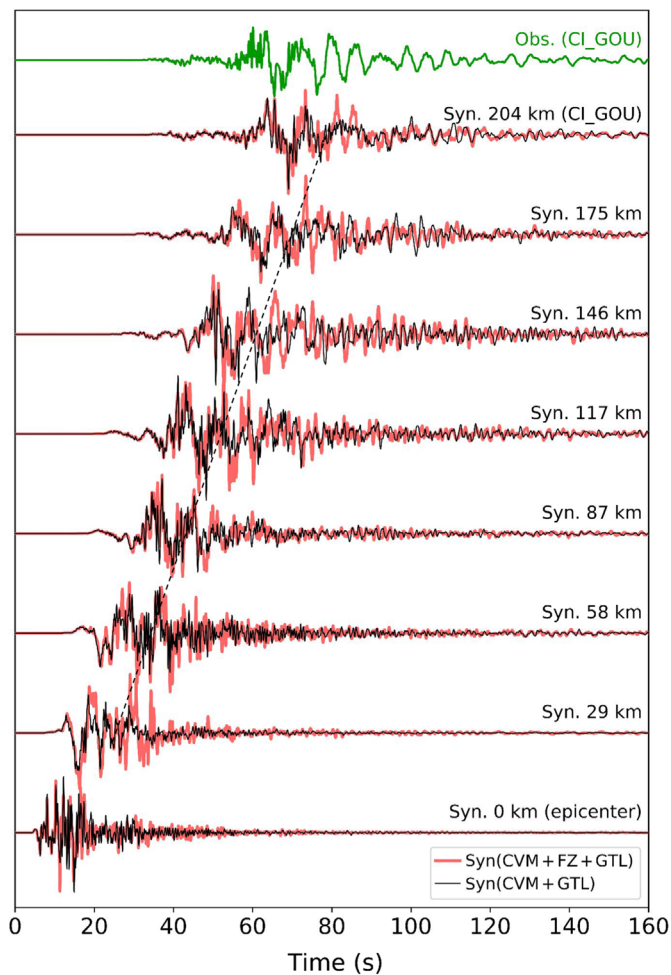


Figure 9. Record sections of the east–west component of synthetic velocity waveforms computed with (thick traces) and without (thin traces) the fault zone compared with the data at station CI_GOU (see Fig. 1a for locations of the epicenter and station CI_GOU). The amplitudes at each distance are normalized by the maximum amplitude of the synthetic waveform computed with the fault zone structure. The dashed line indicates a wavespeed of ~ 3.2 km/s. The color version of this figure is available only in the electronic edition.

an optimal depth of 700 m for a V_{S30} -constrained GTL, as well as values of $k = 0.1$ and $\gamma = 0.5$ for frequency-dependent anelastic attenuation parameterized as $Q_S(f) = Q_{S,0}f^\gamma$, in which $Q_{S,0} = kV_S$. Here, $k = 0.1$ is consistent with the low-frequency Q models estimated by Olsen *et al.* (2003, 2009), Withers *et al.* (2015), Savran and Olsen (2019), Pitarka *et al.* (2021), and Hu *et al.* (2022a,b), and the $Q(f)$ model is within the range determined by Hu *et al.* (2022a). Furthermore, the range of γ estimated in this study is similar to that from seismic observations in southern California. For example, our results are in agreement with the inverted value of 0.4 from the study by Lin and Jordan (2018) using P - and S -wave spectra, $0.5 \leq \gamma \leq 0.8$ from Song and Jordan (2013) constrained by local earthquake data when considering elastic scattering and $\gamma = 0.45$ by

Raof *et al.* (1999) obtained from fitting the spectra of earthquake ground-motion records.

Using the calibrated $Q(f)$ model, we analyzed the effects of the fault zone model on strong ground motions during the 2019 M_w 7.1 Ridgecrest earthquake. Our analysis shows that the fault zone structure significantly affects the predicted ground motions both near the source and south into the Los Angeles basin. When considering the SCEC CVM-S as a reference, our simulations indicate that the fault zone structure improves modeling of the long-period features in the data and lengthens the coda-wave trains in better agreement with observations. The presence of the fault zone structure generates trapped waves and increases near-source ground motions, which is consistent with earlier findings (Ben-Zion and Aki, 1990; Li and Leary, 1990; Ben-Zion *et al.*, 2003; Lewis *et al.*, 2005; Peng and Ben-Zion, 2006). In particular, the fault zone enables the simulations to more accurately reproduce large-amplitude Love waves observed in the data. For example, including the fault zone structure in the velocity model decreases the 0.1–0.5 Hz mean absolute FAS bias to seismic recordings for all sites in the model and in the Los Angeles basin area by 16% and 26%, respectively. We therefore recommend that fault zone structures, if available and constrained by data, be included in future wave propagation simulations for large earthquakes with surface rupture.

DATA AND RESOURCES

The numerical simulations were carried out on Summit at the Oak Ridge Leadership Computing Facility (ORNL). The finite-difference code used in this study (AWP-ODC) can be downloaded from the GitHub repository (<https://github.com/SCECcode/awp>). Model preparation and data processing were done on Andes at ORNL. We used acceleration data from HN channels at stations in the network CI, the Southern California Seismic Network (California Institute of Technology and U.S. Geological Survey Pasadena, 1926); and the network NP, the United States National Strong-Motion Network (U.S. Geological Survey, 1931). Strong-motion seismic data and the corresponding PZ files were accessed using the data fetch tool developed by the Incorporated Research Institutions for Seismology (IRIS), through the web portal of the Southern California Earthquake Data Center at the California Institute of Technology (<http://service.scedc.caltech.edu>). The Seismic Analysis Code from IRIS was used to process the strong-motion data. The kinematic source rupture models of Chen *et al.* (2020), Goldberg *et al.* (2020), and Liu *et al.* (2019) were obtained directly from the authors via personal communication. The supplemental material contains additional figures supporting the discussion in the main article, a description of how the optimal geotechnical layer and $Q(f)$ parameters were determined, and animations of wave propagation. All websites were last accessed in March 2022.

DECLARATION OF COMPETING INTERESTS

The authors acknowledge that there are no conflicts of interest recorded.

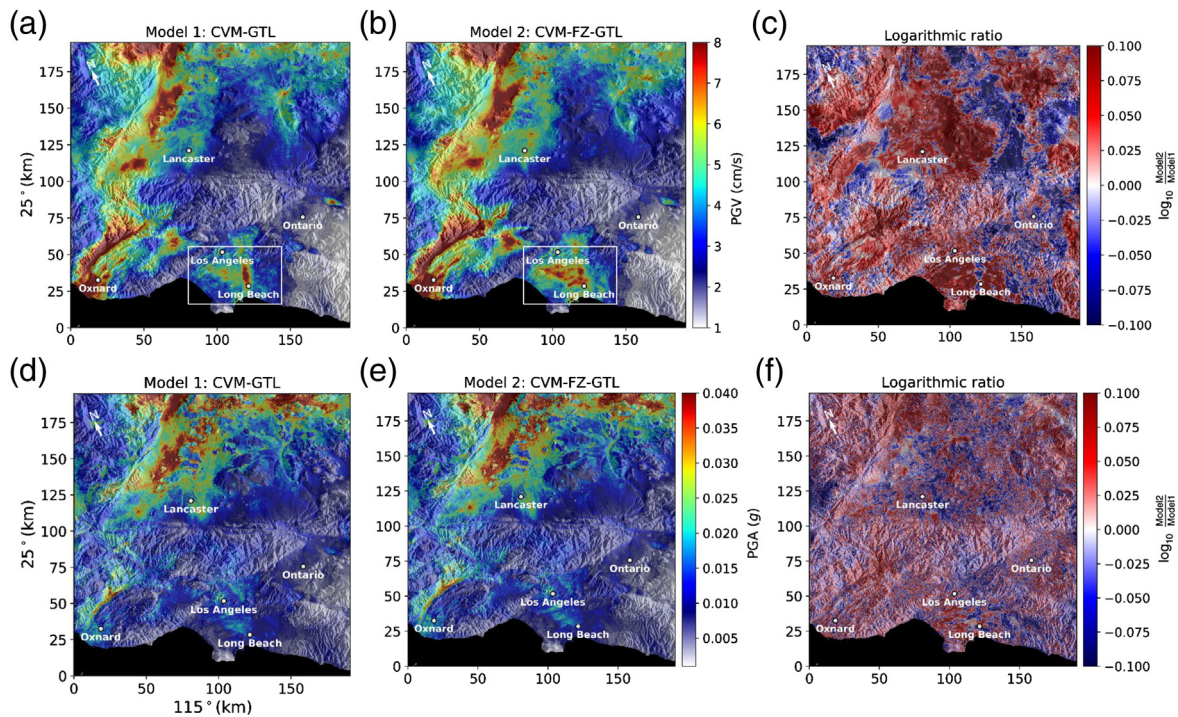


Figure 10. (a,b) PGVs and (d,e) PGAs in the southern portion of the simulation domain (dotted magenta box in Fig. 1a) with (CVM-FZ-GTL) and without (CVM-GTL) the fault zone structure included. The white box

highlights the greater Los Angeles basin area. (c,f) Maps of the ratio between peak motions with and without the fault zone (note log scale). The color version of this figure is available only in the electronic edition.

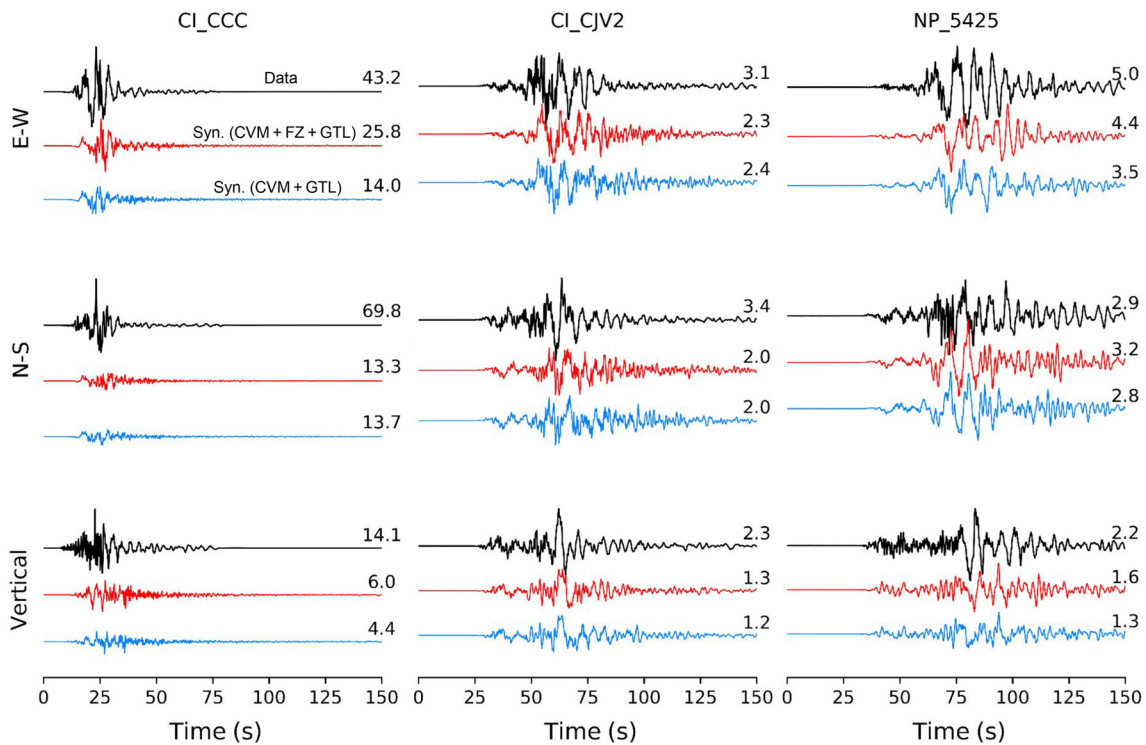


Figure 11. Comparison of observed velocity waveforms on three components with synthetics computed for models CVM + FZ + GTL and CVM + GTL at three different sites. Maximum amplitudes in centimeters per second are

shown to the right of each waveform. See Figure 1 for locations. The color version of this figure is available only in the electronic edition.

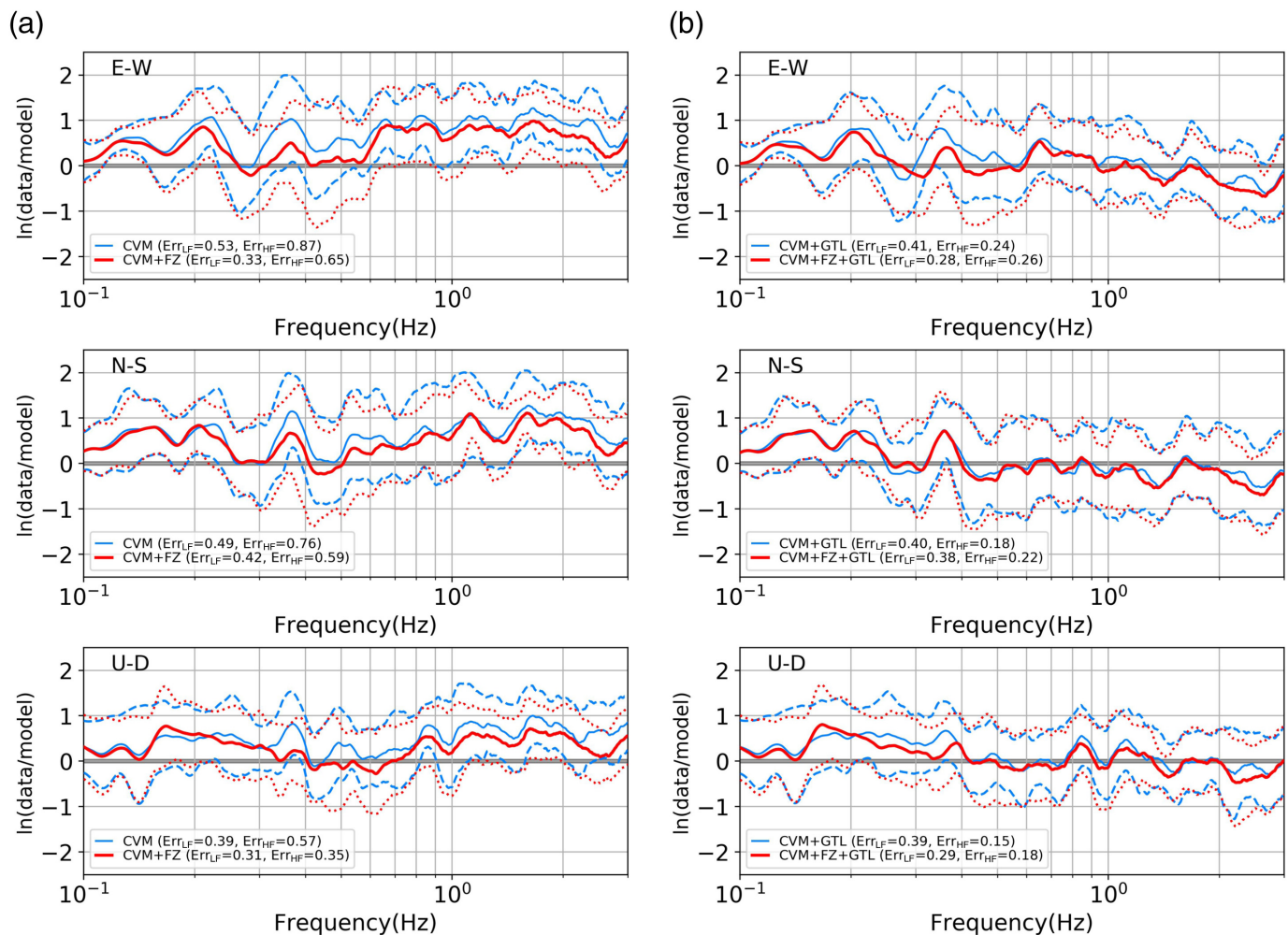


Figure 12. (a) Comparison of the Fourier amplitude spectrum (FAS) GOF curves (see supplementary material, equations S1 and S2) for simulations without (CVM + GTL) and with (CVM + FZ + GTL) the fault zone, where thick solid curves depict the mean GOF_{FAS} , and dashed lines show the corresponding standard deviation. (b) Same as the panel (a), but for simulations including the GTL. Only near-source stations were used (see Fig. 1b for locations). Using equation (S2), the low-frequency (Err_{LF}) and the high-frequency (Err_{HF}) errors were calculated for 0.1–0.5 Hz and 0.5–3.0 Hz, respectively. The color version of this figure is available only in the electronic edition.

ACKNOWLEDGMENTS

This research was supported through the Southern California Earthquake Center (SCEC; Contribution Numbers 20157 and 21111). The SCEC is funded by the National Science Foundation (NSF) Cooperative Agreement EAR-1600087 and the U.S. Geological Survey (USGS) Cooperative Agreement G17AC00047. The authors thank Arthur Rodgers and an anonymous reviewer for their thoughtful comments leading to an improved article.

REFERENCES

- Ajala, R., and P. Persaud (2021). Effect of merging multiscale models on seismic wavefield predictions near the southern San Andreas Fault, *J. Geophys. Res.* **126**, no. 10, e2021JB021915, doi: [10.1029/2021JB021915](https://doi.org/10.1029/2021JB021915).
- Aki, K. (1980). Attenuation of shear-waves in the lithosphere for frequencies from 0.05 to 25 Hz, *Phys. Earth Planet. In.* **21**, no. 1, 50–60, doi: [10.1016/0031-9201\(80\)90019-9](https://doi.org/10.1016/0031-9201(80)90019-9).
- Allam, A., Y. Ben-Zion, I. Kurzon, and F. Vernon (2014). Seismic velocity structure in the Hot Springs and Trifurcation areas of the San Jacinto fault zone, California, from double-difference tomography, *Geophys. J. Int.* **198**, no. 2, 978–999, doi: [10.1093/gji/ggu176](https://doi.org/10.1093/gji/ggu176).
- Ben-Zion, Y., and K. Aki (1990). Seismic radiation from an SH line source in a laterally heterogeneous planar fault zone, *Bull. Seismol. Soc. Am.* **80**, no. 4, 971–994.

- Ben-Zion, Y., Z. Peng, D. Okaya, L. Seeber, J. G. Armbruster, N. Ozer, A. J. Michael, S. Baris, and M. Aktar (2003). A shallow fault-zone structure illuminated by trapped waves in the Karadere–Duzce branch of the North Anatolian Fault, western Turkey, *Geophys. J. Int.* **152**, no. 3, 699–717, doi: [10.1046/j.1365-246X.2003.01870.x](https://doi.org/10.1046/j.1365-246X.2003.01870.x).
- Bianco, M. J., and P. Gerstoft (2018). Travel time tomography with adaptive dictionaries, *IEEE Trans. Comput. Imaging* **4**, no. 4, 499–511, doi: [10.1109/TCL.2018.2862644](https://doi.org/10.1109/TCL.2018.2862644).
- Bianco, M. J., P. Gerstoft, K. B. Olsen, and F.-C. Lin (2019). High-resolution seismic tomography of Long Beach, CA using machine learning, *Sci. Rep.* **9**, no. 1, 14,987, doi: [10.1038/s41598-019-50381-z](https://doi.org/10.1038/s41598-019-50381-z).

- Boore, D. M., and W. B. Joyner (1997). Site amplifications for generic rock sites, *Bull. Seismol. Soc. Am.* **87**, no. 2, 327–341.
- Brocher, T. M. (2005). Empirical relations between elastic wavespeeds and density in the earth's crust, *Bull. Seismol. Soc. Am.* **95**, no. 6, 2081–2092, doi: [10.1785/0120050077](https://doi.org/10.1785/0120050077).
- Brune, J. N. (1970). Tectonic stress and the spectra of seismic shear waves from earthquakes, *J. Geophys. Res.* **75**, no. 2, 4997–5009, doi: [10.1029/JB075i026p04997](https://doi.org/10.1029/JB075i026p04997).
- California Institute of Technology and U.S. Geological Survey Pasadena (1926). Southern California seismic network, doi: [10.7914/SN/CI](https://doi.org/10.7914/SN/CI).
- Catchings, R. D., M. R. Goldman, J. H. Steidl, J. H. Chan, A. A. Allam, C. J. Criley, Z. Ma, D. S. Langermann, G. J. Huddleston, A. T. McEvilly, et al. (2020). Nodal seismograph recordings of the 2019 Ridgecrest earthquake sequence, *Seismol. Res. Lett.* **91**, no. 6, 3622–3633, doi: [10.1785/0220200203](https://doi.org/10.1785/0220200203).
- Chen, K., J.-P. Avouac, S. Aati, C. Milliner, F. Zheng, and C. Shi (2020). Cascading and pulse-like ruptures during the 2019 Ridgecrest earthquakes in the Eastern California Shear Zone, *Nat. Commun.* **11**, no. 1, 22, doi: [10.1038/s41467-019-13750-w](https://doi.org/10.1038/s41467-019-13750-w).
- Cochran, E. S., Y.-G. Li, P. M. Shearer, S. Barbot, Y. Fialko, and J. E. Vidale (2009). Seismic and geodetic evidence for extensive, long-lived fault damage zones, *Geology* **37**, no. 4, 315–318.
- Cui, Y., K. B. Olsen, T. H. Jordan, K. Lee, J. Zhou, P. Small, D. Roten, G. Ely, D. K. Panda, A. Chourasia, et al. (2010). Scalable earthquake simulation on petascale supercomputers, *SC '10: Proceedings of the 2010 ACM/IEEE International Conference for High Performance Computing, Networking, Storage and Analysis*, New Orleans, Louisiana, 13–19 November 2010, 1–20, doi: [10.1109/SC.2010.45](https://doi.org/10.1109/SC.2010.45).
- Cui, Y., E. Poyraz, K. B. Olsen, J. Zhou, K. Withers, S. Callaghan, J. Larkin, C. Guest, D. Choi, A. Chourasia, Z. Shi, S. M. Day, P. J. Maechling, and T. H. Jordan (2013). Physics-based seismic hazard analysis on petascale heterogeneous supercomputers, *SC '13: Proceedings of the International Conference on High Performance Computing, Networking, Storage and Analysis*, 17 November 2013, 1–12, doi: [10.1145/2503210.2503300](https://doi.org/10.1145/2503210.2503300).
- Ely, G. P., T. Jordan, P. Small, and P. J. Maechling (2010). A VS30-derived near-surface seismic velocity model, *2010 American Geophysical Union Annual Meeting*, San Francisco, California, 13 December 2010.
- Fohrmann, M., H. Igel, G. Jahnke, and Y. Ben-Zion (2004). Guided waves from sources outside faults: An indication for shallow fault zone structure? *Pure Appl. Geophys.* **161**, no. 11, 2125–2137, doi: [10.1007/s00024-004-2553-y](https://doi.org/10.1007/s00024-004-2553-y).
- Goldberg, D. E., D. Melgar, V. J. Sahakian, A. M. Thomas, X. Xu, B. W. Crowell, and J. Geng (2020). Complex rupture of an immature fault zone: A simultaneous kinematic model of the 2019 Ridgecrest, CA earthquakes, *Geophys. Res. Lett.* **47**, no. 3, e2019GL086382, doi: [10.1029/2019gl086382](https://doi.org/10.1029/2019gl086382).
- Graves, R., and A. Pitarka (2016). Kinematic ground-motion simulations on rough faults including effects of 3D stochastic velocity perturbations, *Bull. Seismol. Soc. Am.* **106**, no. 5, 2136–2153, doi: [10.1785/0120160088](https://doi.org/10.1785/0120160088).
- Hirakawa, E., and A. J. Barbour (2020). Kinematic rupture and 3D wave propagation simulations of the 2019 Mw 7.1 Ridgecrest, California, earthquake, *Bull. Seismol. Soc. Am.* **110**, no. 4, 1644–1659, doi: [10.1785/0120200031](https://doi.org/10.1785/0120200031).
- Hu, Z., K. B. Olsen, and S. M. Day (2022a). 0–5 Hz deterministic 3-D ground motion simulations for the 2014 La Habra, California, earthquake, *Geophys. J. Int.* **230**, no. 3, 2162–2182, doi: [10.1093/gji/ggac174](https://doi.org/10.1093/gji/ggac174).
- Hu, Z., K. B. Olsen, and S. M. Day (2022b). Calibration of the near-surface seismic structure in the SCEC community velocity model version 4, *Geophys. J. Int.* **230**, no. 3, 2183–2198, doi: [10.1093/gji/ggac175](https://doi.org/10.1093/gji/ggac175).
- Igel, H., G. Jahnke, and Y. Ben-Zion (2002). Numerical simulation of fault zone guided waves: Accuracy and 3-D effects, in *Earthquake Processes: Physical Modelling, Numerical Simulation and Data Analysis Part I*, M. Matsu'ura, P. Mora, A. Donnellan, and X.-C. Yin (Editors), 2067–2083, Birkhäuser Basel, Basel, Switzerland.
- Lai, V. H., R. W. Graves, C. Yu, Z. Zhan, and D. V. Helmberger (2020). Shallow basin structure and attenuation are key to predicting long shaking duration in Los Angeles Basin, *J. Geophys. Res.* **125**, no. 10, e2020JB019663, doi: [10.1029/2020JB019663](https://doi.org/10.1029/2020JB019663).
- Lewis, M. A., Z. Peng, Y. Ben-Zion, and F. L. Vernon (2005). Shallow seismic trapping structure in the San Jacinto fault zone near Anza, California, *Geophys. J. Int.* **162**, no. 3, 867–881, doi: [10.1111/j.1365-246X.2005.02684.x](https://doi.org/10.1111/j.1365-246X.2005.02684.x).
- Li, Y.-G., P. Leary, K. Aki, and P. Malin (1990). Seismic trapped modes in the Oroville and San Andreas Fault Zones, *Science* **249**, no. 4970, 763–766, doi: [10.1126/science.249.4970.763](https://doi.org/10.1126/science.249.4970.763).
- Li, Y.-G., and P. C. Leary (1990). Fault zone trapped seismic waves, *Bull. Seismol. Soc. Am.* **80**, no. 5, 1245–1271, doi: [10.1785/BSSA0800051245](https://doi.org/10.1785/BSSA0800051245).
- Li, Y.-G., J. E. Vidale, and E. S. Cochran (2004). Low-velocity damaged structure of the San Andreas Fault at Parkfield from fault zone trapped waves, *Geophys. Res. Lett.* **31**, no. 12, doi: [10.1029/2003GL019044](https://doi.org/10.1029/2003GL019044).
- Lin, Y.-P., and T. H. Jordan (2018). Frequency-dependent attenuation of P and S waves in Southern California, *J. Geophys. Res.* **123**, no. 7, 5814–5830, doi: [10.1029/2018jb015448](https://doi.org/10.1029/2018jb015448).
- Liu, C., T. Lay, E. E. Brodsky, K. Dascher-Cousineau, and X. Xiong (2019). Coseismic rupture process of the large 2019 Ridgecrest earthquakes from joint inversion of geodetic and seismological observations, *Geophys. Res. Lett.* **46**, no. 21, 11,820–11,829, doi: [10.1029/2019GL084949](https://doi.org/10.1029/2019GL084949).
- Nie, S., Y. Wang, K. B. Olsen, and S. M. Day (2017). Fourth-order staggered-grid finite-difference seismic wavefield estimation using a discontinuous mesh interface (WEDMI) fourth-order staggered-grid finite-difference seismic WEDMI, *Bull. Seismol. Soc. Am.* **107**, no. 5, 2183–2193, doi: [10.1785/0120170077](https://doi.org/10.1785/0120170077).
- Olsen, K., and R. Takedatsu (2014). The SDSU Broadband Ground-Motion Generation Module BToolbox Version 1.5, *Seismol. Res. Lett.* **86**, no. 1, 81–88, doi: [10.1785/0220140102](https://doi.org/10.1785/0220140102).
- Olsen, K. B. (1994). Simulation of three-dimensional wave propagation in the Salt Lake Basin, *Ph.D. Thesis*, University of Utah, Salt Lake City, Utah, 157 pp.
- Olsen, K. B., S. M. Day, and C. R. Bradley (2003). Estimation of Q for long-period (>2 sec) waves in the Los Angeles Basin, *Bull. Seismol. Soc. Am.* **93**, no. 2, 627–638, doi: [10.1785/0120020135](https://doi.org/10.1785/0120020135).
- Olsen, K. B., S. M. Day, L. A. Dalguer, J. Mayhew, Y. Cui, J. Zhu, V. M. Cruz-Atienza, D. Roten, P. Maechling, T. H. Jordan, et al. (2009). ShakeOut-D: Ground motion estimates using an ensemble of large

- earthquakes on the southern San Andreas Fault with spontaneous rupture propagation, *Geophys. Res. Lett.* **36**, no. 4, doi: [10.1029/2008GL036832](https://doi.org/10.1029/2008GL036832).
- O'Reilly, O., T. Yeh, K. B. Olsen, Z. Hu, A. Breuer, D. Roten, and C. A. Goulet (2021). A high-order finite-difference method on staggered curvilinear grids for seismic wave propagation applications with topography, *Bull. Seismol. Soc. Am.* **112**, no. 1, 3–22, doi: [10.1785/0120210096](https://doi.org/10.1785/0120210096).
- Peng, Z., and Y. Ben-Zion (2006). Temporal changes of shallow seismic velocity around the Karadere-Düzce branch of the north Anatolian fault and strong ground motion, *Pure Appl. Geophys.* **163**, no. 2, 567–600.
- Phillips, W. S., K. M. Mayeda, and L. Malagnini (2014). How to invert multi-band, regional phase amplitudes for 2-D attenuation and source parameters: Tests using the USArray, *Pure Appl. Geophys.* **171**, no. 3, 469–484, doi: [10.1007/s00024-013-0646-1](https://doi.org/10.1007/s00024-013-0646-1).
- Pitarka, A., R. Graves, K. Irikura, K. Miyakoshi, C. Wu, H. Kawase, A. Rodgers, and D. McCallen (2021). Refinements to the Graves–Pitarka kinematic rupture generator, including a dynamically consistent slip-rate function, applied to the 2019 Mw 7.1 Ridgecrest earthquake, *Bull. Seismol. Soc. Am.* **112**, no. 1, 287–306, doi: [10.1785/0120210138](https://doi.org/10.1785/0120210138).
- Raouf, M., R. B. Herrmann, and L. Malagnini (1999). Attenuation and excitation of three-component ground motion in southern California, *Bull. Seismol. Soc. Am.* **89**, no. 4, 888–902, doi: [10.1785/bssa0890040888](https://doi.org/10.1785/bssa0890040888).
- Roten, D., K. B. Olsen, S. M. Day, and Y. Cui (2018). Quantification of fault-zone plasticity effects with spontaneous rupture simulations, in *Best Practices in Physics-based Fault Rupture Models for Seismic Hazard Assessment of Nuclear Installations*, L. A. Dalguer, Y. Fukushima, K. Irikura, and C. Wu (Editors), Springer International Publishing, Cham, Switzerland, 45–67.
- Roten, D., K. B. Olsen, S. M. Day, Y. Cui, and D. Fäh (2014). Expected seismic shaking in Los Angeles reduced by San Andreas fault zone plasticity, *Geophys. Res. Lett.* **41**, no. 8, 2769–2777, doi: [10.1002/2014GL059411](https://doi.org/10.1002/2014GL059411).
- Savran, W. H., and K. B. Olsen (2019). Ground motion simulation and validation of the 2008 Chino Hills earthquake in scattering media, *Geophys. J. Int.* **219**, no. 3, 1836–1850, doi: [10.1093/gji/ggz399](https://doi.org/10.1093/gji/ggz399).
- Scott, J. S., T. G. Masters, and F. L. Vernon (1994). 3-D velocity structure of the San Jacinto fault zone near Anza, California—I. P waves, *Geophys. J. Int.* **119**, no. 2, 611–626, doi: [10.1111/j.1365-246X.1994.tb00145.x](https://doi.org/10.1111/j.1365-246X.1994.tb00145.x).
- Small, P., D. Gill, P. J. Maechling, R. Tabor, S. Callaghan, T. H. Jordan, K. B. Olsen, G. P. Ely, and C. Goulet (2017). The SCEC unified community velocity model software framework, *Seismol. Res. Lett.* **88**, no. 6, 1539–1552, doi: [10.1785/0220170082](https://doi.org/10.1785/0220170082).
- Song, X., and T. Jordan (2013). Anelastic attenuation and elastic scattering of seismic waves in the Los Angeles region, *2013 American Geophysical Union Annual Meeting*, San Francisco, California, 9 December 2013, Vol. 2013, S32B–05.
- Spudich, P., and K. B. Olsen (2001). Fault zone amplified waves as a possible seismic hazard along the Calaveras Fault in central California, *Geophys. Res. Lett.* **28**, no. 13, 2533–2536, doi: [10.1029/2000GL011902](https://doi.org/10.1029/2000GL011902).
- Tabor, R., S. Azzadeh-Roodpish, N. Khoshnevis, and K. Cheng (2016). Evaluation of the southern California seismic velocity models through simulation of recorded events, *Geophys. J. Int.* **205**, no. 3, 1342–1364, doi: [10.1093/gji/ggw085](https://doi.org/10.1093/gji/ggw085).
- Tabor, R., and J. Bielak (2013). Ground-motion simulation and validation of the 2008 Chino Hills, California, earthquake, *Bull. Seismol. Soc. Am.* **103**, no. 1, 131–156, doi: [10.1785/0120110325](https://doi.org/10.1785/0120110325).
- Tabor, R., and J. Bielak (2014). Ground-motion simulation and validation of the 2008 Chino Hills, California, earthquake using different velocity models, *Bull. Seismol. Soc. Am.* **104**, no. 4, 1876–1898, doi: [10.1785/0120130266](https://doi.org/10.1785/0120130266).
- U.S. Geological Survey (1931). United States national strong-motion network, doi: [10.7914/SN/NP](https://doi.org/10.7914/SN/NP).
- Vidale, J. E., and Y.-G. Li (2003). Damage to the shallow Landers fault from the nearby Hector mine earthquake, *Nature* **421**, no. 6922, 524–526.
- Wald, D. J., and T. I. Allen (2007). Topographic slope as a proxy for seismic site conditions and amplification, *Bull. Seismol. Soc. Am.* **97**, no. 5, 1379–1395, doi: [10.1785/0120060267](https://doi.org/10.1785/0120060267).
- Wang, K., D. S. Dreger, E. Tinti, R. Bürgmann, and T. Taira (2020). Rupture process of the 2019 Ridgecrest, California Mw 6.4 foreshock and Mw 7.1 earthquake constrained by seismic and geodetic data, *Bull. Seismol. Soc. Am.* **110**, no. 4, 1603–1626, doi: [10.1785/0120200108](https://doi.org/10.1785/0120200108).
- Wang, R., B. Schurr, C. Milkereit, Z. Shao, and M. Jin (2011). An improved automatic scheme for empirical baseline correction of digital strong-motion records, *Bull. Seismol. Soc. Am.* **101**, no. 5, 2029–2044, doi: [10.1785/0120110039](https://doi.org/10.1785/0120110039).
- Wang, W., and P. M. Shearer (2017). Using direct and coda wave envelopes to resolve the scattering and intrinsic attenuation structure of Southern California, *J. Geophys. Res.* **122**, no. 9, 7236–7251, doi: [10.1002/2016jb013810](https://doi.org/10.1002/2016jb013810).
- Withers, K. B., K. B. Olsen, and S. M. Day (2015). Memory-efficient simulation of frequency-dependent QMemory-efficient simulation of frequency-dependent Q, *Bull. Seismol. Soc. Am.* **105**, no. 6, 3129–3142, doi: [10.1785/0120150020](https://doi.org/10.1785/0120150020).
- Yong, A., A. Martin, K. Stokoe, and J. Diehl (2013). *ARRA-funded VS30 measurements using multi-technique approach at strong-motion stations in California and central-eastern United States*, U.S. Geol. Surv. Open-File Rept. 2013-1102, U.S. Department of the Interior, 60 p. and data files.
- Zhou, Z., M. Bianco, P. Gerstoft, and K. Olsen (2022). High-resolution imaging of complex shallow fault zones along the July 2019 Ridgecrest ruptures, *Geophys. Res. Lett.* **49**, no. 1, e2021GL095024, doi: [10.1029/2021GL095024](https://doi.org/10.1029/2021GL095024).

Manuscript received 30 November 2022

Published online 26 April 2023